GeoScienceWorld
Lithosphere
Volume 2022, Article ID 1796297, 20 pages
https://doi.org/10.2113/2022/1796297

Lithosphere

Research Article

Gas-Bearing Property in Deep Marine Shale and Its Micro Controlling Factors: Evidence from the Lower Silurian Longmaxi Formation in Southern Sichuan, China

Xin Wang,[1,2,3] Jianhui Zeng,[1,2] Jinhui Chen,[4,5] Zhenxue Jiang,[1,3] Zixin Xue,[1,3] Xiangye Kong,[1,2,3] Qianyou Wang,[1,3] and Kunkun Jia[1,2]

[1]*State Key Laboratory of Petroleum Resources and Prospecting, China University of Petroleum, Beijing 102249, China*
[2]*College of Geosciences, China University of Petroleum, Beijing 102249, China*
[3]*Unconventional Natural Gas Institute, China University of Petroleum, Beijing 102249, China*
[4]*School of Public Policy and Management, Tsinghua University, Beijing 100084, China*
[5]*High-Tech Research and Development Center, Ministry of Science and Technology, Beijing 100044, China*

Correspondence should be addressed to Jianhui Zeng; zengjh@cup.edu.cn and Jinhui Chen; chenjinhui@mail.tsinghua.edu.cn

Received 31 May 2022; Revised 7 October 2022; Accepted 15 October 2022; Published 19 November 2022

Academic Editor: Jingwei Huang

The gas content in shale reservoirs is often determined by the micro storage and sealing capacities of the reservoir. Deep shale reservoirs are in the high- or over-thermale maturity stage and have complex pore structure and connectivity, which are highly heterogeneous in vertical distribution. Research on the gas-bearing property of deep shale reservoirs is limited by these complex microscopic conditions. To analyze the gas-bearing characteristics of deep shale reservoirs, this work collected and summarized data on total organic carbon content, mineral composition, porosity, water saturation, and gas content measured on-site for the Longmaxi Formation in the Sichuan Basin in southern Sichuan, China. Then, experimental methods, such as X-ray photoelectron spectroscopy, transmission electron microscope, low-pressure N_2 adsorption, spontaneous imbibition, and high-pressure methane adsorption, were used to analyze the micro storage and sealing capacities of the deep shale reservoirs. The results show that, different from shallow shale reservoirs (<3500 m), deep shale reservoirs have a higher graphitization degree and water saturation. An abundance of graphite structures often leads to weak resistance of organic matter to compression, deformation, or even collapse of pores in organic matter and severe damage to the gas storage space. However, a higher degree of graphitization can enhance the ability of the shale reservoirs to adsorb gas and self-sealing. The high water saturation in the reservoirs can interact with clay minerals and negatively affect the gas accumulation, storage, and transmission capacities of the shale reservoirs. However, the upper shale reservoirs with higher water saturation can seal the lower shale reservoirs, helping it preserve shale gas. Based on the vertical distribution of graphite structure, clay minerals contents, lithofacies, and water content in deep shale reservoirs, the essential microscopic conditions for deep shale reservoirs to have high gas content were proposed. This paper provides a detailed explanation and evaluation of deep shale's storage and sealing capacities at the microscopic scale and can serve as a reference for further identifying the patterns for high-yield and rich shale gas reservoirs and improving deep shale gas exploration technologies.

1. Introduction

As a rock with extremely low porosity and permeability, shale was once not considered a cost-efficient target [1–4]. However, with the application and promotion of horizontal well hydraulic fracturing, micro-seismic monitoring, multi-well industrialized exploitation, and other technologies, both North America and China have currently industrialized the development of shale gas exploitation in formations with a buried depth of fewer than 3,500 meters [2, 5], which provides comprehensive knowledge about their sedimentary [6], developmental characteristics of fractures [7], pore

structure [3, 8], gas-bearing characteristics [9, 10], and these factors' effects on shale gas differential accumulation [11]. In addition, models of shale gas accumulation and dispersion under different reservoir-forming conditions have been established [11–13]. Moreover, with the continued improvement of exploitation technologies in recent years, deep shale reservoirs (burial depth > 3500 m) also have shown great potential and attracted the attention of petroleum geologists [14–16].

More recently, geologists' research on shale oil and gas has gradually evolved from macro- to micro-scale [17–19]. There are often complex pore networks in organic-rich shales, comprising numerous pore types [8, 20], complex pore geometric shapes [8, 20], and wide pore size distribution [3, 20, 21]. The ways by which shale gas accumulates and transmits may vary with the pore size. Generally, the gas transport is dominated by bulk flow in macro-pores, which provide space for free gas, and by slip flow and surface diffusion in tiny pores, which provide larger surface area and higher adsorption energy for adsorbed gas [19]. The characterization of pore structure is crucial for understanding the storage and transport mechanisms of shale gas [21, 22]. For deeper shale reservoirs, their higher thermal maturity and more complex pore structures can complicate the shale gas occurrence and transmission mechanism [15, 21]. As a result, the microfactors affecting shale gas accumulation in these deep shale reservoirs remain unclear.

The Sichuan Basin is the largest hydrocarbon-bearing superimposed basin in the Yangtze Plate [23–25]. The Lower Silurian Longmaxi Formation in the southern Sichuan Basin is a shale gas reservoir formed by fine-grained marine sediments and had witnessed a continuous subsidence stage before the Late Jurassic and an uplift stage after the Late Jurassic [26]. The subsequent relatively mild uplift and modification led to a stable structure and minor faults in southern Sichuan [27]. The sedimentary rocks of the Longmaxi Formation in southern Sichuan are mainly distributed at a depth ≥ 3500 m [15]. They are high- or overmatured thermally, with a R_o value up to 3.5% [15]. High thermal evolution often means complex pore structure and highly heterogeneous pore spatial distribution [21]. These microscopic factors have caused many risks in deep shale exploration. Therefore, to better understand the reservoir quality and gas-bearing capacity and provide help for dessert evaluation, a micro-scale gas storage-preservation system is an aiming target in this research. Only in this way, studies on deep shale gas enrichment can proceed smoothly.

In this paper, primary data measured on-site were collected and summarized to analyze the basic and gas-bearing characteristics of the deep shale reservoirs in southern Sichuan, including the total organic carbon (TOC) content, mineral composition, porosity, water saturation (S_w), and gas content. Then, experimental methods, such as X-ray photoelectron spectroscopy (XPS), transmission electron microscope (TEM), low-pressure N_2 adsorption, spontaneous imbibition (SI), and high-pressure methane adsorption, were used to identify the micro controlling factors of gas-bearing properties. Then, the graphite structure development, pore structure, connectivity, and methane adsorption of deep shale reservoirs were discussed, with the controlling factors of the micro-storage capacity and micro-sealing capacity of these shale reservoirs analyzed. Using stratigraphic correlation and based on on-site gas content and production data, the vertical distribution of graphite structure, mineral composition, and water content in deep shale reservoirs was determined, and the essential microscopic conditions for deep shale reservoirs to realize high gas content were proposed. The microcontrolling factors of gas-bearing properties were illustrated, laying a theoretical foundation for identifying the high-yield and enrichment patterns of shale gas and supporting future research on deep shale gas exploration technology.

2. Geological Settings

The Sichuan Basin is a superimposed basin developed based on the Yangtze Craton [24, 28]. Located in the northwest of the Upper Yangtze region, it is rich in oil and gas resources [24]. The features of the large structures in the Upper Yangtze Platform had shaped the Sichuan Basin as a NE-trending diamond (Figure 1(a)). The frequent and violent tectonic activities of the Platform had resulted in an internal structure of the Basin with multiple cycles, multistage tectonism, and multilevel tectonic control [28]. Based on its multilevel structure, the Basin can be divided into six structural units [29]: Eastern Sichuan fold belt, Southern Sichuan fold belt, Northern Sichuan low and flat fold belt, Western Sichuan low and slightly sloping fold belt, Central Sichuan slightly sloping fold belt, and Southwestern Sichuan low and slightly sloping fold belt. This study focused on the southern part of the Sichuan Basin, mainly the shale gas reservoirs distributed in the Southern Sichuan fold belt and Southwestern Sichuan low and slightly sloping fold belt (Figure 1(a)).

During the Late Ordovician and Early Silurian, a significant transgression occurred due to the melting of glaciers in southern Sichuan, leading to the transition from the Ordovician carbonate sedimentary system to the clastic sedimentary system [30, 31]. This left fine-grained clastic sediments on the early deposited carbonate rocks [30, 31]. The Late Ordovician Wufeng Formation is dominated by carbonaceous and siliceous shales, while the Early Silurian Longmaxi Formation is dominated by black carbonaceous and gray-black sandy shales [25]. The Longmaxi Formation shales are now buried throughout southern Sichuan from dozens of meters to 6000 m below ground (Figure 1(b)) [15]. The shallow shale reservoir is at the edge of the Basin, with shales buried at a depth of fewer than 3,500 m or even exposed on the ground in areas where intense uplifts have occurred. This is the main development base of shale gas in China [24]. The deep shale reservoir is inside the Basin, with shales buried at a depth of over 3,500 m. It is an important target for future deep shale gas exploration in China [32].

The Longmaxi Formation can be vertically divided into the Longmaxi-1 member (LF), Longmaxi-2 member (LS), and Longmaxi-3 member (LT) according to the lithology and graptolite development (Figure 1(c)) [31]. With a thickness of about 30-120 m, LF is composed of black

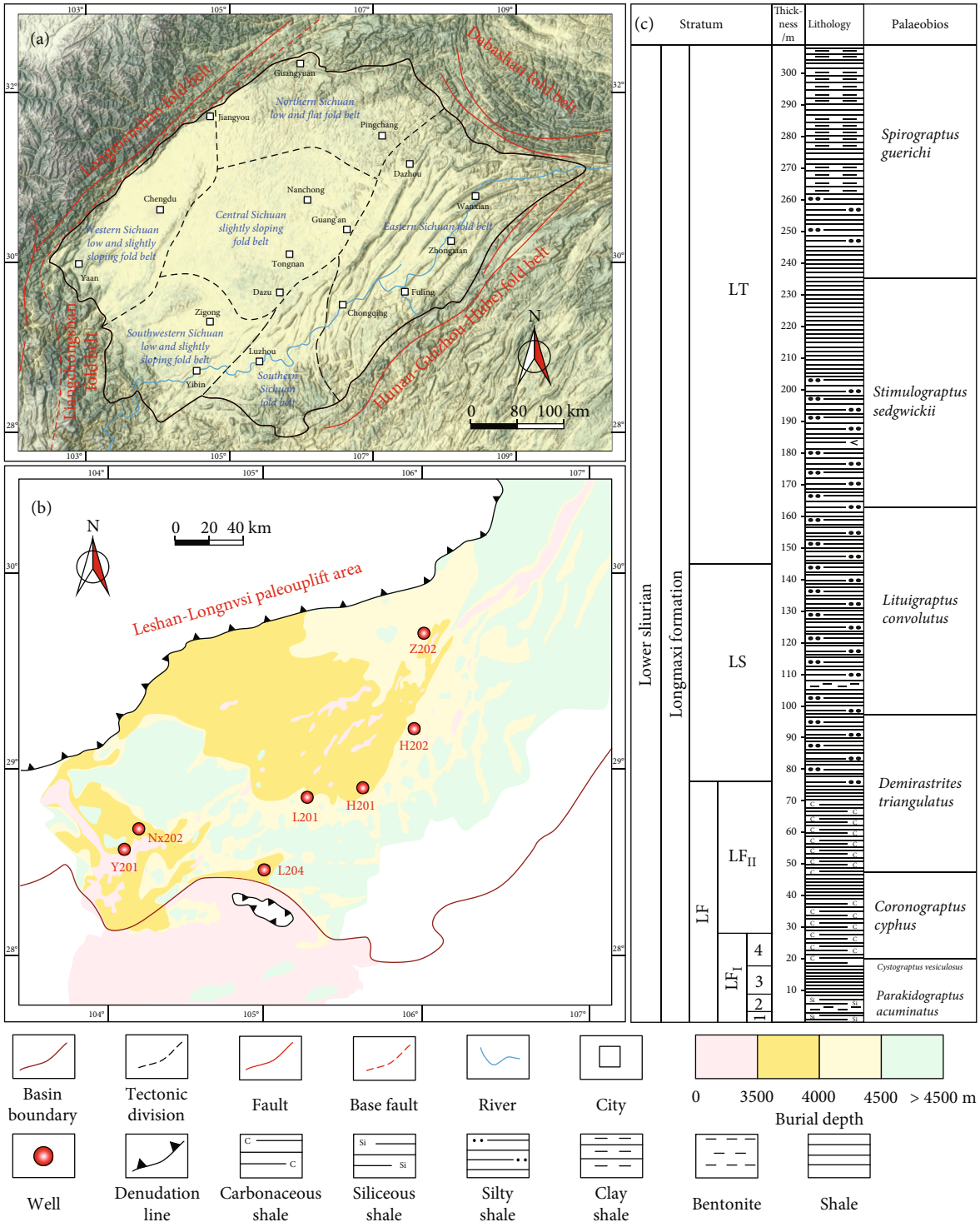

FIGURE 1: (a) Tectonic unit division of the Sichuan Basin [29], (b) buried depth map of Longmaxi Formation in southern Sichuan Basin and the regions for the development of deep shale gas [15], and (c) comprehensive stratigraphic column of Longmaxi Formation in southern Sichuan Basin [31–34].

carbonaceous, siliceous, and dark gray silty shales and is rich in graptolite and organic matter [31]. LF can be further subdivided into LF_I and LF_{II} (Figure 1(c)) [31–34]. Deep shale reservoir LF_I is distributed stably and continuously in the horizontal direction, with slight variation in formation thickness from the edge to the center of the Basin, and is a major shale gas development section with a continuous large area [32]. LF_I can be further divided into the first layer (LF_I^1), second layer (LF_I^2), third layer (LF_I^3), and fourth layer (LF_I^4). The thickness differs greatly between these layers, increasing from the basin edge to the basin center [33, 34].

Table 1: Strata, depth, R_o, water content, clay minerals contents, and porosity of deep shale samples.

Samples ID	Well	Strata	Depth (m)	R_o (%)	Water content (mg/g)	Clay minerals (%)	Porosity (%)
1	Nx202	LF_I^4	3904.88	3.17	40.28	30.4	1.6
2	Nx202	LF_I^3	3920.26	3.11	41.35	33.0	2.3
3	Nx202	LF_I^2	3931.43	3.21	55.11	25.6	1.5
4	Nx202	LF_I^1	3938.53	3.19	36.96	14.5	2.2
5	Nx202	LF_I^1	3939.44	3.19	33.70	16.9	2.1
6	L204	LF_I^1	3842.67	2.91	40.57	25.9	3.8
7	L204	LF_I^1	3843.1	2.91	18.68	17.2	5.4
8	H201	LF_I^1	4122.8	2.94	64.02	29.7	6.1
9	H202	LF_{II}	3913.54	2.84	59.81	55.6	3.2
10	H202	LF_I^4	4032.3	2.91	80.25	41.5	4.3
11	H202	LF_I^3	4044.69	2.88	91.24	43.3	4.3
12	H202	LF_I^2	4063.77	2.94	53.60	33.2	3.9
13	H202	LF_I^1	4077.85	2.94	50.87	29.2	4.0

3. Samples, Data, and Experimental Methods

3.1. Samples and Data Source. On-site measurements of seven deep shale gas wells (Y201, Nx202, L204, H201, L201, H202, and Z202, Figure 1(b)) were collected, including TOC, R_o, mineral composition, porosity, S_w, and gas content data. All on-site measurements were provided by PetroChina Southwest Oil and Gas field Company (SWOG). In addition, thirteen shale samples were collected from seven deep shale gas wells in southern Sichuan (Table 1). Low-pressure nitrogen adsorption analyses and spontaneous dialysis (SI) were conducted to identify the pore structure characteristics and connectivity of the thirteen shale samples. Eight samples were selected for transmission electron microscopy (TEM) observation and XPS experiment to analyze the graphite structure in the studied deep shale reservoir. The same eight shale samples were moisture-equilibrated, and then, methane adsorption at high temperature and high pressure was conducted to determine their methane adsorption capacity.

3.2. X-Ray Photoelectron Spectroscopy (XPS). With increased maturity and the loss of functional groups with oxygen, sulfur, and nitrogen, organic carbonaceous matters will lose their structure and gradually evolve from disordered to ordered graphite-like ones [35]. X-ray photoelectron spectroscopy (XPS) can analyze the organic material on the sample surface and provide information on elemental composition, the element's chemical state and molecular structure [36]. A Thermo Fisher K-alpha XPS system was used in this paper. Before the analysis, to extract shale organic matter, the ground shale samples (<80 mesh) were treated with hydrochloric acid, hydrofluoric acid, sodium hydroxide, and other reagents, respectively. After the test, the C1s peak was corrected with 284.8 eV as the reference. Then, the 4.1 version of XPSPEAK was used for peak fitting. The relative content of graphite was calculated based on the binding energy of graphite, C-C, and C-O bonds, and the organic matter's degree of graphitization was quantified based on the peak ratio. This test was used to provide direct evidence for the existence of graphite structure in deep shales.

3.3. Transmission Electron Microscope (TEM). After understanding the evolution pattern of molecular structures of organic matter during thermal evolution, the transmission electron microscope (TEM) was used to directly observe the organic matter in the low-resistance shale. TEM can be used to observe the lattice or vertical stacking features of crystal structures with ordered crystal form, and there will also be distinct diffraction spots of lattice during secondary diffraction. For example, TEM can be used to directly observe the lattice morphological characteristics of graphitized organic matter with layered structure and regular crystal form [37]. When an electron beam is applied, graphite crystals produce elastically scattered electrons, resulting in regular and clear diffraction spots on the TEM image. In contrast, the nongraphitized organic matter is anisotropic and has no fixed regular forms internally. It also shows diffused rings after electron bombardment, and no prominent patterns can be found on the TEM image.

3.4. Low-Pressure N_2 Adsorption. Powder samples (80 to 100 mesh) of approximately 1 to 2 g were prepared using standard cores. To remove adsorbed moisture and volatile substances, the samples were automatically degassed at 110°C under vacuum for about 14 hours. Low pressure (<0.127 MPa) N_2 adsorption analysis was performed using a Micromeritics® Tristar II 3020 Analyzer. The relative pressure (P/P0) for N_2 adsorption ranged from 0.001 to 0.995. Adsorption isotherms were generated by the analyzer automatically based on theories of adsorption. Meanwhile, the pore diameter followed the Brunauer-Emmett-Teller (BET) model [38], and the pore volume and specific surface area (SSA) were calculated following the Barrett-Joyner-Halenda (BJH) model [39].

3.5. Spontaneous Imbibition (SI). Spontaneous imbibition (SI) is a capillary force-controlled process, during which the wet phase displaces the nonwet phase only by capillary

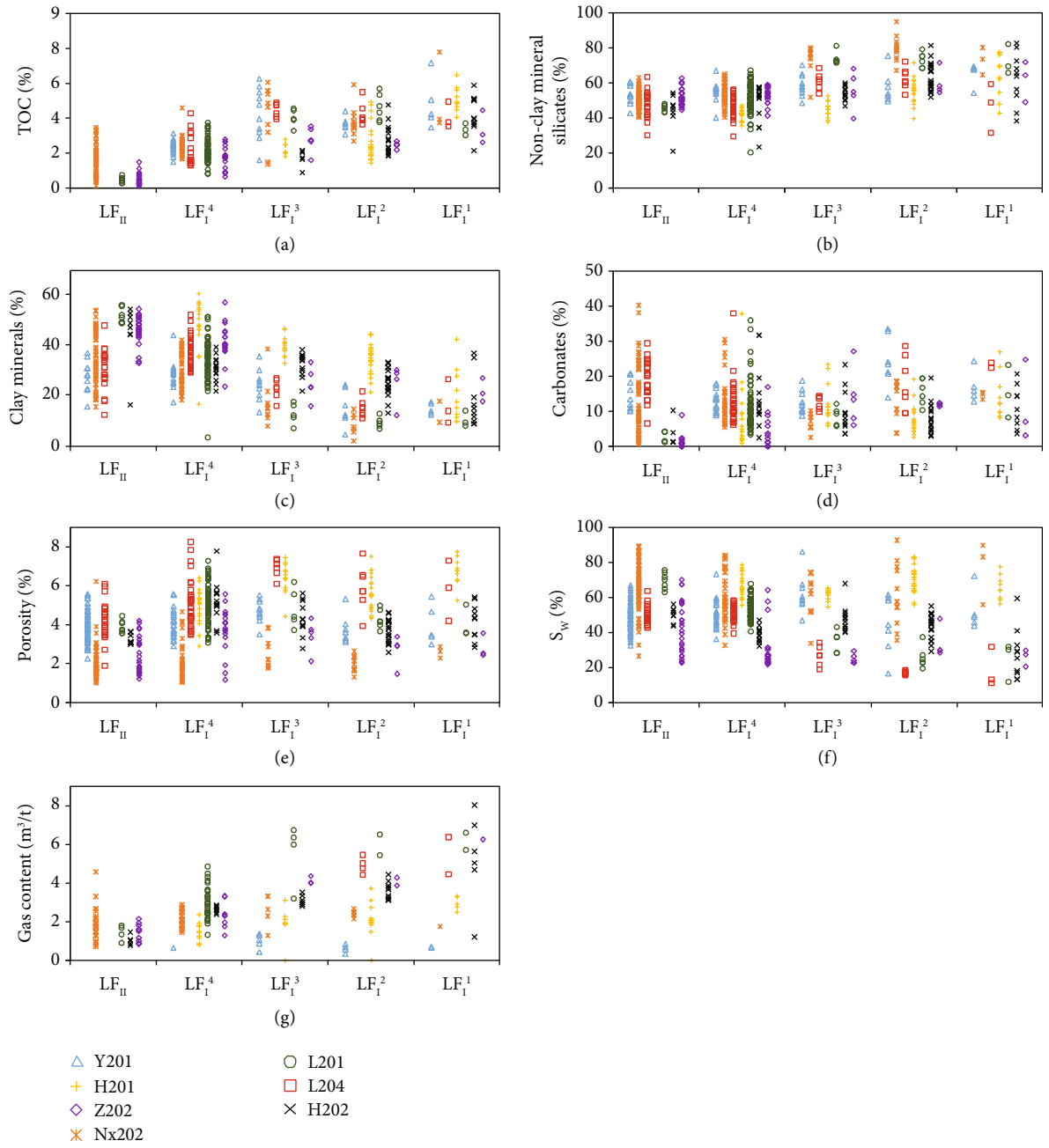

FIGURE 2: Reservoir basic characteristics of typical deep shale gas wells in southern Sichuan Basin. (a) TOC content in each layer, (b) contents of nonclay mineral silicates in each layer, (c) contents of clay minerals in each layer, (d) contents of carbonates in each layer, (e) porosity in each layer, (f) S_w in each layer, and (g) gas content in each layer.

pressure. Cube samples with a side length of 1 cm were prepared using the standard cores. Then, all faces (except the top and bottom ones) were coated with fast-curing clear epoxy resin. Water were used as absorption fluids to replace the nonwet phase air. Spontaneous imbibition direction is vertical to bedding. To ensure the consistency of initial S_w, all samples were dried at 60°C (140°F) for at least 48 hours before SI tests. The schematic diagram, experimental procedure, and data processing method of the SI experiment were described in detail in previous studies by Gao and Hu [40].

3.6. High-Pressure Methane Adsorption. The method and instrument for determining methane adsorption capacity of shale samples were mainly based on the experience with coal samples. A high-pressure isothermal adsorption system (Rubotherm, Germany) which can generate an adsorption pressure of up to 50 MPa was used. The powdered shale samples (<60 mesh) were moisture-equilibrated. Equilibrium moisture content was reached in a vacuum desiccator using the saturated solution of K_2SO^4 at 97% relative humidity. Samples were weighed every 24 hours until a constant weight was reached. The high-pressure methane adsorption tests

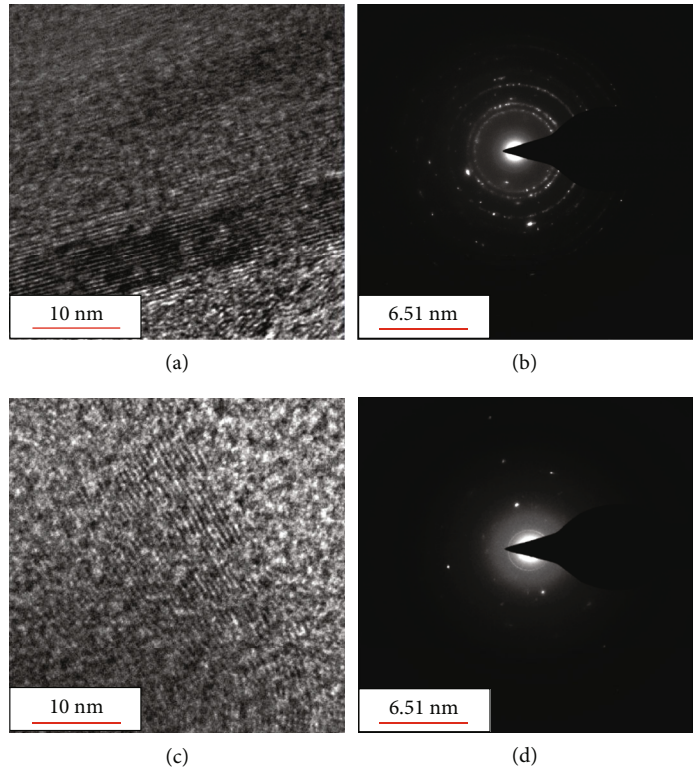

Figure 3: The TEM images and diffraction images of deep shales at different maturity evolution stages. (a) TEM image of sample 5, (b) diffraction image of sample 5, (c) TEM image of sample 8, and (d) diffraction image of sample 8.

were carried out at a constant temperature of 100°C and with gradually increased pressure. The amount of adsorbed methane under different pressures was recorded using a volumetric method. Ji et al. [10] described the detailed process of the high-pressure methane adsorption experiment in their study. Due to its simplicity and suitability for our measured data, the ternary Langmuir equation for high-pressure cases was used to fit our data and determine the Langmuir parameters.

4. Results

4.1. Basic Geological Features

4.1.1. Total Organic Carbon. A total of 456 TOC data for the seven deep shale gas wells were collected (Figure 2(a)). The TOC content of LF_I ranges between 0.66% and 7.80%, with an average of 2.90%. About 75% of samples have a TOC value higher than 2%, showing a good hydrocarbon generation potential. The TOC content of LF_{II} ranges between 0.11% and 3.45%, with an average of 1.22%. Vertically, the organic matter abundance of deep shale increases gradually from LF_{II} to LF_I^1, with the overall TOC content of LF_I^1 higher than 2%. The TOC content and its spatial distribution of deep shale reservoirs are similar to those of shallow shale reservoirs (at a burial depth of 2,262 m ~2,589 m) [29].

4.1.2. Mineral Components. The mineral components data of 513 deep shale samples (Figures 2(b)–2(d)) show that the deep shales are mainly composed of non-clay mineral silicates (quartz, orthoclase, and plagioclase) and clay minerals (Figures 2(b) and 2(c)). The contents of non-clay mineral silicates are generally high (Figure 2(b)), ranging from 20.2% to 98.5%, with an average of 54.1%. Vertically, the contents of non-clay mineral silicates gradually increase from LF_{II} to LF_I^2, reach a peak in LF_I^2, and then show a slight fall in LF_I^1. The contents of clay minerals are low in general (Figure 2(c)), ranging from 1.60% to 60.29%, with an average of 31.42%. Vertically, the clay mineral contents are similar between LF_{II} and LF_I^4, ranging from 3% to 60.29%, with an average of 36.81%. Then, from LF_I^3 to LF_I^1, the clay mineral contents drop sharply, ranging from 1.6% to 46.43%, with an average of 23.04%. Compared with the clay minerals contents of shallow shale reservoirs (at a burial depth of 2,262 m ~2,589 m) [29], the clay mineral contents in the deep shale shows a significant difference between the upper layers (LF_{II} and LF_I^4) and the lower layers (LF_I^3 to LF_I^1). It does not show a slow and continued drop with the formation depth increasing. The carbonates are the lowest (Figure 2(d)), ranging from 0% to 40.3%, with an average of 11.93%. No significant pattern is observed in the spatial distribution of carbonates.

4.1.3. Porosity. Based on 589 data (Figure 2(e)), the porosity of the deep shales ranges between 0.99% and 8.26%, with an average of 3.67%. The proportion of porosity with a value greater than 5% reaches 25.13%. The porosity of deep shale reservoirs is lower than that of shallow shale reservoirs (at a burial depth of 2,262 m ~2,589 m) [29]. From LF_{II} to LF_I^1, the porosity range of each layer is 0.99% ~6.22%, 1.05% ~8.26%, 1.77% ~7.46%, 1.30% ~7.66%,

Table 2: XPS test results for eight deep shale samples.

Sample ID	Well	Strata	Chemical construction	Binding energy (eV)	Peak area	FWHM (eV)	L/G (%)	Relative content (%)
2	Nx202	LF_I^3	C-O, C=O	285.315	20667.35	2.972	20	29.15
			C-C	284.772	36420.07	0.954	20	51.38
			Graphite	284.300	13806.08	0.990	20	19.47
3	Nx202	LF_I^2	C-O, C=O	285.122	18657.06	2.526	20	28.70
			C-C	284.757	32132.77	0.952	20	49.42
			Graphite	284.300	14222.65	0.912	20	21.88
5	Nx202	LF_I^1	C-O, C=O	285.266	17298.81	2.878	20	27.23
			C-C	284.765	30511.65	0.971	20	48.04
			Graphite	284.300	15709.90	0.912	20	24.73
6	L204	LF_I^1	C-O, C=O	285.413	18889.61	3.153	20	32.45
			C-C	284.794	28623.44	0.973	20	49.17
			Graphite	284.300	10697.93	0.990	20	18.38
8	H201	LF_I^1	C-O, C=O	285.790	15656.53	2.210	20	27.63
			C-C	285.033	31409.55	0.884	20	55.43
			Graphite	284.300	9600.055	0.963	20	16.94
10	H202	LF_I^4	C-O, C=O	285.374	24230.19	2.032	20	36.11
			C-C	284.835	36976.61	1.022	20	55.09
			Graphite	284.300	5902.37	1.445	20	8.80
12	H202	LF_I^2	C-O, C=O	285.386	23682.30	1.344	20	42.14
			C-C	284.868	26071.79	0.954	20	46.38
			Graphite	284.300	6451.29	1.203	20	11.48
13	H202	LF_I^1	C-O, C=O	285.429	25813.62	1.790	20	40.70
			C-C	284.894	30206.88	0.958	20	47.63
			Graphite	284.300	7399.39	1.379	20	11.67

Table 3: Total pore volume, total specific surface area, and average pore diameter for thirteen deep shale samples.

Sample ID	Well	Strata	TPV (cm^3/g)	TSSA (m^2/g)	APD (nm)
1	Nx202	LF_I^4	0.01579	17.59	5.06
2	Nx202	LF_I^3	0.02370	27.12	4.67
3	Nx202	LF_I^2	0.01299	17.75	4.42
4	Nx202	LF_I^1	0.01273	16.92	4.49
5	Nx202	LF_I^1	0.01623	24.58	4.14
6	L204	LF_I^1	0.02811	26.29	5.52
7	L204	LF_I^1	0.01739	12.42	6.91
8	H201	LF_I^1	0.03455	35.66	5.22
9	H202	LF_{II}	0.04418	34.23	13.38
10	H202	LF_I^4	0.03737	30.88	7.08
11	H202	LF_I^3	0.03359	25.50	7.81
12	H202	LF_I^2	0.02963	20.56	7.62
13	H202	LF_I^1	0.02706	26.48	5.47

and 2.29% ~7.76%, respectively, showing discrete and irregular spatial distribution. Though the porosity distribution of a single well shows some prominent patterns, the porosity of different wells peaks at different layers. The porosity of Well Y201 and L204 peaks at LF_I^3; for Wells Nx202 and H201, it peaks at LF_I^3 and LF_I^1; and for Wells L201, H202, and Z202, it peaks at LF_I^4.

4.1.4. Water Saturation. A total of 589 on-site data (Figure 2(f)) show that the S_w of deep shales ranges between

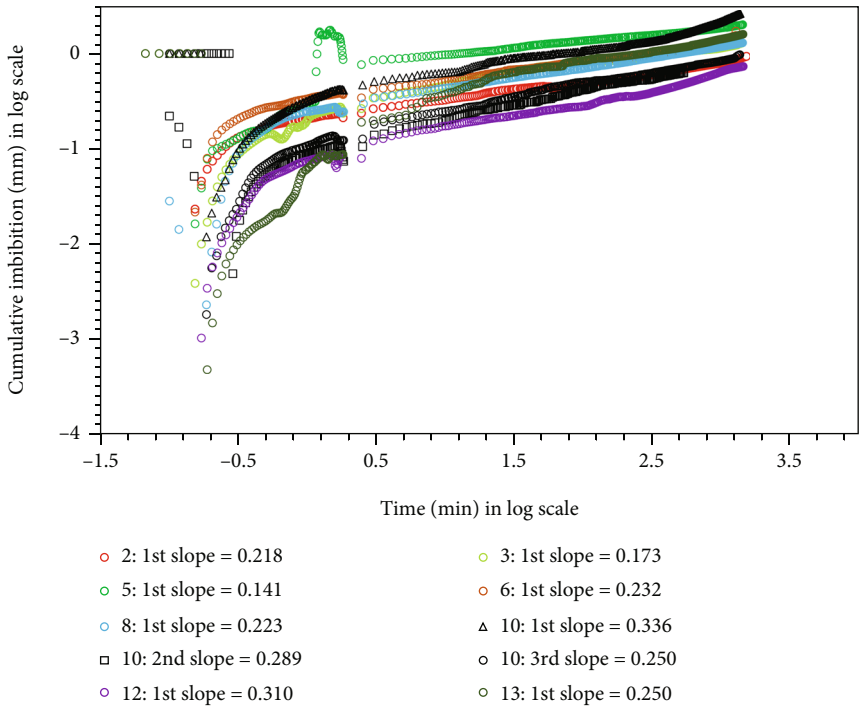

Figure 4: Cumulative imbibition height vs. imbibition time for eight deep shale samples. Three spontaneous imbibition experiments were carried out on sample 10, and only one spontaneous imbibition experiment was carried out on other samples.

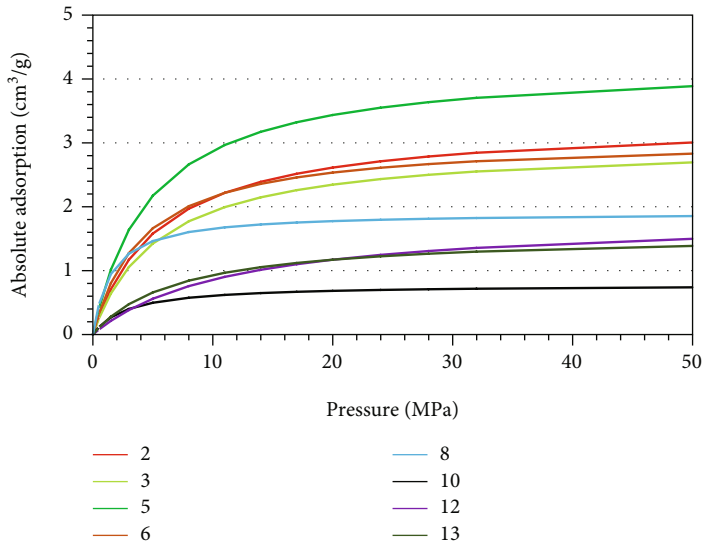

Figure 5: Methane adsorption isotherms for eight deep shale samples.

11.17% and 92.75%, with an average of 52.22%. The proportion of S_w with a value greater than 30% registers at 89.81%, indicating that the deep shale reservoirs are highly S_w. The vertical distribution of S_w varies among wells. The data points of Well Y202, Nx202, and H201 are discrete, and no prominent pattern is observed in the S_w distribution from LF_{II} to LF_I^1. The S_w for Well L204, L201, H202, and Z202 is concentrated in a narrow range, and the S_w decreases continuously from LF_{II} to LF_I^1. The S_w of the deep shale reservoir is higher than that of shallow shale reservoirs (at a burial depth of 2,262 m ~2,589 m) [29].

4.1.5. Gas Content. Based on a total of 198 data (Figure 2(g)), the gas content of seven wells ranges between 0.35 m^3/t and 8.04 m^3/t, with an average of 2.69 m^3/t. From LF_{II} to LF_I^1, the gas content average of each layer is 1.65 m^3/t, 2.44 m^3/t, 2.88 m^3/t, 2.99 m^3/t, and 4.16 m^3/t, respectively, showing an increase with burial depth. There are significant differences

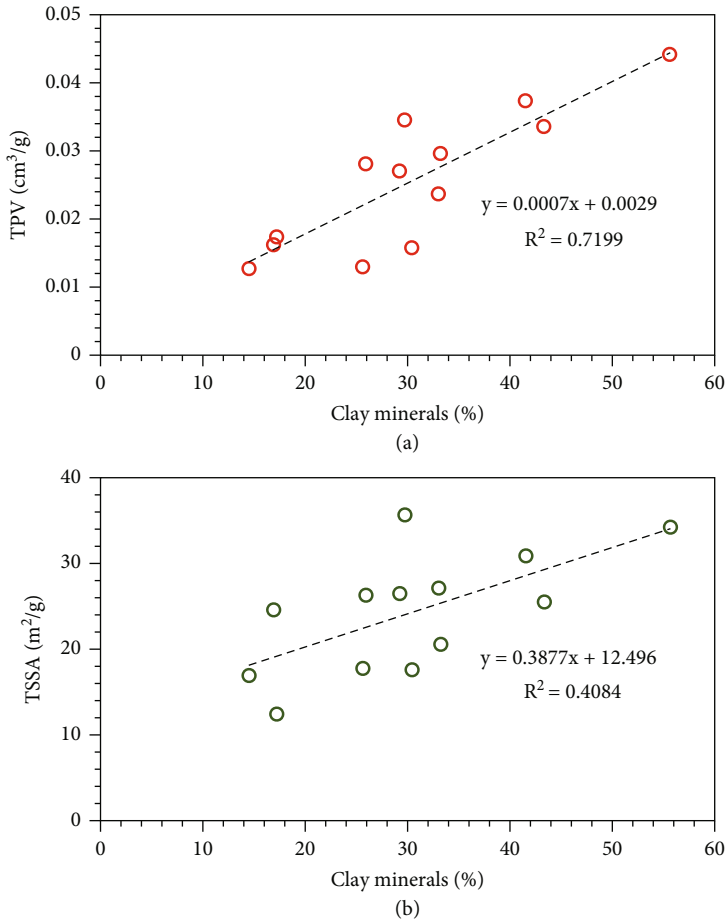

Figure 6: (a) Total pore volume and (b) total specific surface area vs. contents of clay minerals.

among wells. The gas content of Wells Y201, Nx202, and H201 is low, ranging from 0.19 m^3/t to 4.58 m^3/t, with an average of 0.81 m^3/t, 2.07 m^3/t, and 2.10 m^3/t, respectively. The gas content of Wells L204, L201, H202, and Z202 is higher, ranging from 0.86 m^3/t ~8.04 m^3/t, with an average of 4.716 m^3/t, 3.30 m^3/t, 3.22 m^3/t, and 2.71 m^3/t, respectively. The gas content of the deep shale reservoir is lower than that of shallow shale reservoirs (at a burial depth of 2,262 m ~2,589 m) [29].

4.2. Graphitization of Organic Matter. The organic matter in deep shales shows high thermal maturity and is in the high- or over-maturity stage (Table 1). The TEM technique was used to observe the extracted organic matter from eight deep shale samples. A large number of regular layered structures are found (Figures 3(a) and 3(c)), and their crystal forms are similar to those of graphite. A large number of ring-shaped diffraction spots are found (Figures 3(b) and 3(d)), with distinct lattice features, which is the typical graphite pattern. Graphitization of organic matter occurs in these shales in general. The TEM images and diffraction images of deep shales at different thermal evolution stages (Figure 3) show that layered and striped graphitized lattices in organic matter increase with a higher degree of maturity and so does the continuity of graphitization. The diffraction images also show that the point-shaped monocrystals increase with the thermal evolution, indicating the increase of monocrystal graphite.

Table 2 shows the XPS fitting results of carbon peaks for LF_I shale samples from different wells. For shale organic matter of varying maturity, the intensities of their representative peaks of C-O bonds, C-C bonds, and Π bonds differ significantly. Although with different relative content, graphite structures are found in the organic matter of all eight samples, indicating the common existence of graphite structures in the organic matter of deep shale reservoirs. The relative content of graphitic structure in organic matter increases from the basin center to the edge (Figure 1(b) and Table 2). The relative content of graphite structure is highest in the LF_I^1 sample from Well Nx202, reaching 24.73%; and it is relatively lower in the LF_I^1 sample from Well H202, dropping to 11.67%. Vertically, for Well Nx202 and H202, the relative content of graphitic structure in organic matter gradually increases from LF_I^4 to LF_I^1.

4.3. Micro pores in Deep Shale Reservoir

4.3.1. Characteristics of Pore Structures. As shown in Table 3, the total pore volume (TPV), total specific surface area (TSSA), and average pore diameter (APD) were obtained

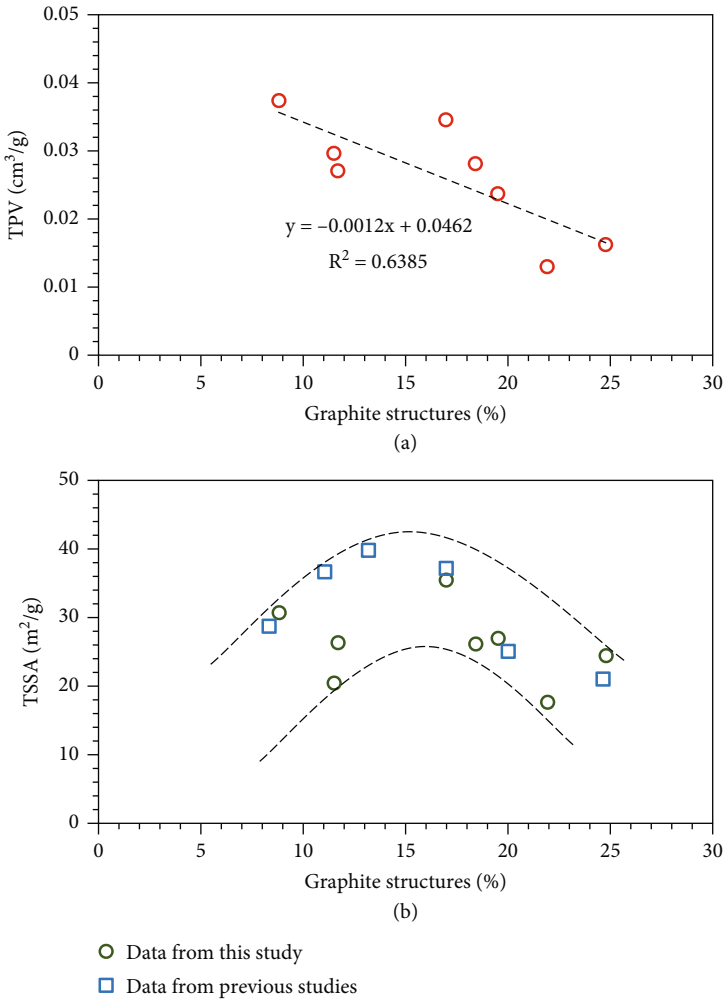

Figure 7: (a) Total pore volume and (b) total specific surface area vs. the relative content of graphite structures. The data of the blue square is from Xue et al. [36].

using low-temperature N_2 adsorption isotherms. Its TPV ranges from 0.01273 to 0.04418 cm^3/g, with an average of 0.02564 cm^3/g; its TSSA ranges from 12.42 to 35.66 m^2/g, with an average of 24.31 m^2/g; and its APD is 4.14~13.38 nm, with an average of 6.29 nm. Compared with the shallow shale reservoirs of the Longmaxi Formation in the Fuling area [29], the deep shale reservoir shows a larger pore volume and specific surface area.

4.3.2. Pore Connectivity. SI experiments were made on 8 deep shale reservoir samples. During the first 30 seconds of each SI experiment, the samples were unstable as they sank into the fluid, causing fluctuations in weight (Figure 4). Then, the cumulative SI height showed a linear relationship with SI duration. The slope (or ratio) between the cumulative SI height and SI duration on a logarithmic scale is shown in Figure 4. According to Handy's equation [41], a theoretical imbibition slope of 0.5 indicates good pore connectivity of the porous medium for the tested fluid, and a lower slope (<0.5) may indicate poor pore connectivity [40].

The pore connectivity varies significantly among the different samples from LF_I^1 (Figure 4). The first-experiment SI slope of the samples from Wells Nx202 and H202 gradually decreased from LF_I^4 to LF_I^1, indicating that the pore connectivity of upper layers is better than that of the lower layers. For the three repeated experiments of 10 samples from LF_I^4, the SI slope gradually falls from 0.336 to 0.250, indicating that the pore connectivity of the samples is affected by the fluid with the increase in the number of experiments.

4.4. Adsorption Characteristics of Deep Shale Gas. The methane adsorption isotherm under high pressure of deep shale samples is shown in Figure 5. The Langmuir volume of deep shale samples ranges between 0.78 and 4.26 m^3/t, and their Langmuir pressure is between 1.53 and 11.45 MPa. For the methane adsorption capacity under moisture-equilibrated conditions, there are significant differences among samples from different depths. Compared with the LF_{II} and LF_I shale reservoirs in southeastern Chongqing (at a burial depth of 655.8 m ~887.1 m), the deep shale reservoirs show a greater

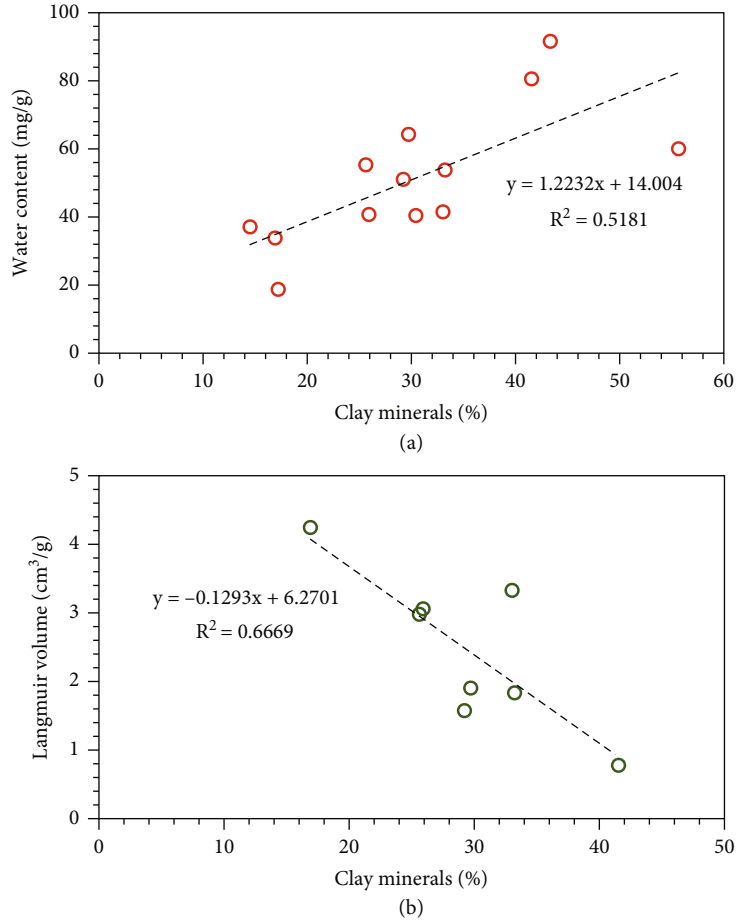

Figure 8: (a) Water content and (b) Langmuir volume vs. contents of clay minerals.

methane adsorption capacity under moisture-equilibrated conditions [42].

5. Discussion

5.1. Gas Storage Capacity of Deep Shale Reservoirs

5.1.1. Contribution of Clay Minerals to Deep Shale Gas Storage Space. Clay minerals are commonly found in marine shale [23, 25]. Unlike other minerals, clay minerals show layered structures built up from silicon-oxygen tetrahedrons and aluminum-oxygen octahedrons, where atoms are arranged with fixed patterns [43, 44]. This layered structure enables the formation of grid- or strip-like interlayer intragranular pores [8, 45]. Moreover, during the transformation of clay minerals, the interlayer dehydration can cause small-scale interlayer collapse and lattice rearrangement, making the flaky clay minerals to form new intercrystalline pores [20]. So, the existence of clay minerals is often accompanied by the massive development of pores. Clay mineral pores have a diameter of 2 ~ 100 nm and a specific surface area of 32.1 m^2/g ~219 m^2/g [8]. With large pore volume and specific surface area, these pores bring valid space for the accumulation and storage of shale gas. As shown in Figure 6, under dry conditions, the TPV and TSSA increase significantly with higher clay minerals contents. It indicates that pores increase in deep shale with the enrichment of clay minerals, which also provides massive space for the storage of fluids in deep shale.

5.1.2. Effect of Graphitization on the Storage Space in Deep Shale. During the thermal evolution of organic matter, carbonaceous matter tends to show an ordered structure [46, 47]. And carbon atom structure transforms from chain to ring, and the aromatic structures increase, eventually transforming into layered graphite structures [46, 47]. The carbon atoms in the graphite structure are linked by α bonds and can withstand deformation under external forces by twisting the chemical bonds [48, 49]. In such a way, with the increase of graphite structures, the ability of organic matter to resist deformation weakens. Deep shale is often under immense pressure from upper formations, and its graphitized organic matter is subject to extrusion and susceptible to plastic deformation [48, 49]. The organic matter pores of the shale of the LF in the Sichuan Basin account for 10~40% of the TPV [50]. The organic matter pores provide the prominent accumulation and storage space for shale gas, and their change can significantly impact on the TPV of shale. The relationship between the TPV and the relative content of graphite structures in the deep shale samples under dry

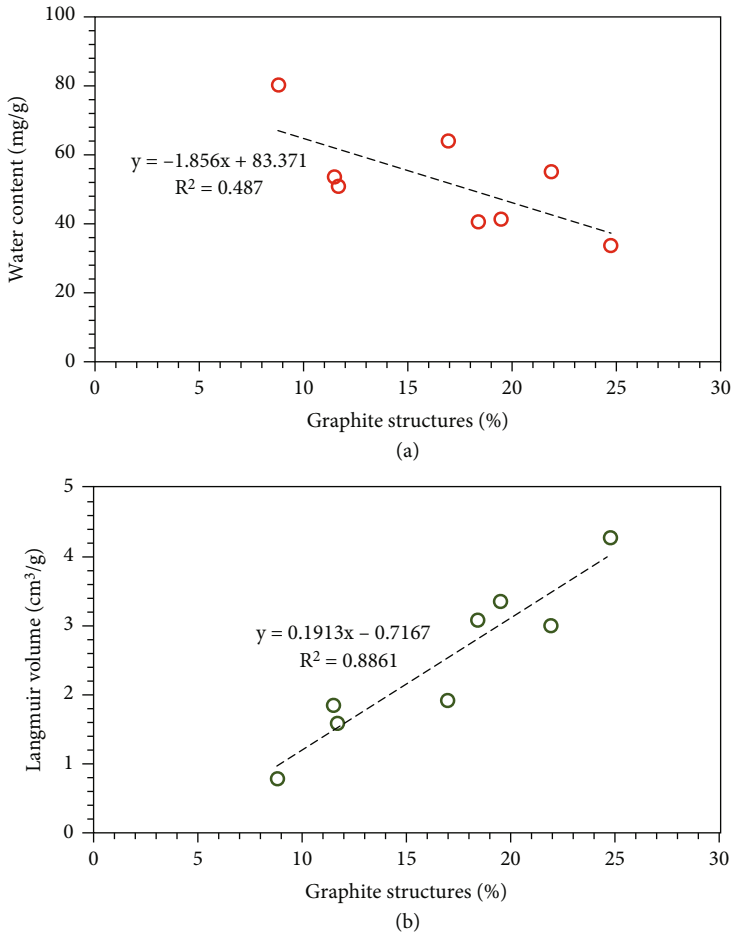

Figure 9: (a) Water content and (b) Langmuir volume vs. content of the relative content of graphite structures.

conditions shows that, with the increase of graphite structures in the organic matter, the TVP decreases significantly (Figure 7(a)). While the organic matter is squeezed and deformed, the pores in the organic matter are also squeezed and twisted, or even collapsed, resulting in a decrease in the number and size of organic matter pores. The graphitization of organic matter can cause severe damage to deep shale pores. Different from the TPV, under dry conditions, as the relative content of graphite structures increases, the TSSA of deep shale samples increases first and then decreases (Figure 7(b)). A possible explanation is that, when the relative content of graphite structures is low, the pores in the organic matter become more minor subject to compression deformation. The proportion of smaller pores in shale increases, and the surface area becomes more extensive [36]. When the relative content of graphite structures is high, the pores in the organic matter collapse or close, resulting in a smaller surface area in shale.

5.1.3. Effect of Water on the Storage Space in Deep Shale. Water in shale reservoirs often occupies the storage space for natural gas [51]. So S_w can directly affect the content of natural gas. For clay minerals pores, with higher contents of clay minerals, the shale pore surface area, as well as the adsorption sites for pore fluid increases, thus improves the shale's adsorption capacity for pore fluid [51]. The atomic replacement of clay minerals can lead to uneven distribution of surface charge, increasing the affinity of the surface of clay minerals to different adsorbates in shale reservoirs [52]. Shale reservoirs usually contain water in natural geological conditions [25, 51]. Compared with shallow shales at a depth less than 3,500 m underground, deep shale cores show a higher water content ranging from 18.68 mg/g to 91.24 mg/g, which increases with the higher contents of clay minerals (Figure 8(a)). Study shows that, for water-saturated shale samples, the methane adsorption decreases by 63.7% to 81.3% when the contents of clay minerals increase [42]. In shale with high S_w, the polar adsorption sites on the surface of clay minerals are often occupied by polar water molecules, negatively affecting the gas adsorption. The relationship between the Langmuir's volume and the contents of clay minerals when shale samples are moisture-equilibrated shows that the methane adsorption capacity decreases with the higher contents of clay minerals (Figure 8(b)). One possible explanation is that tiny pores are blocked by water molecules and thus cannot adsorb methane molecules. The water molecules can form a film on the surface of large pores, hampering the adsorption capacity of the surface to methane molecules. In this way, water significantly inhibits the ability of clay minerals in deep shale reservoirs to adsorb methane.

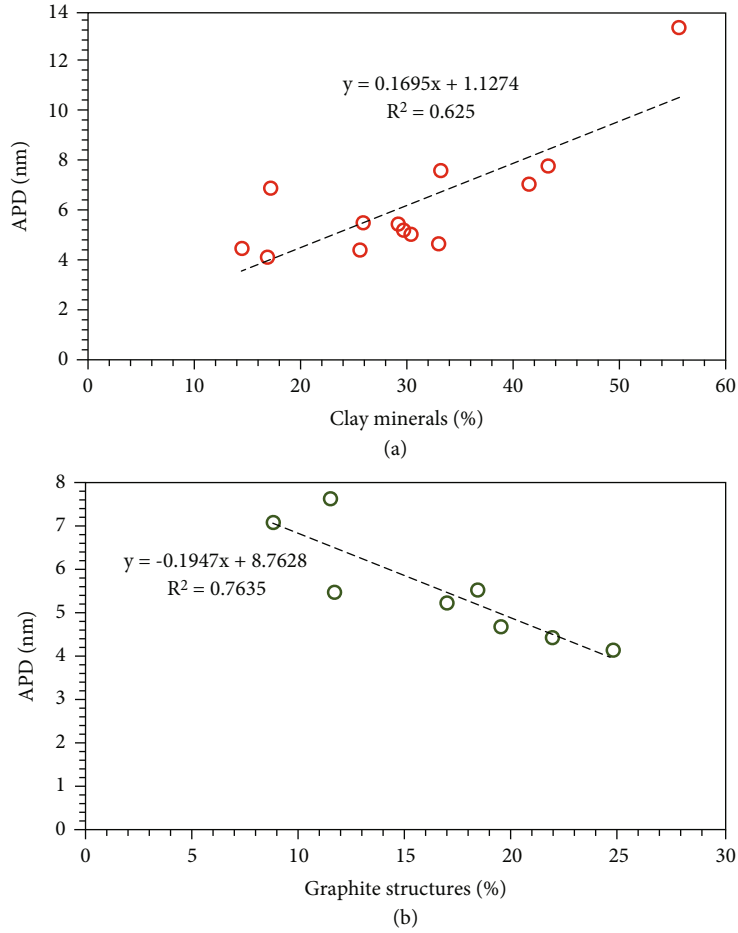

Figure 10: Average pore diameter vs. contents of (a) clay mineral and (b) the relative content of graphite structures.

For the pores in organic matter, with the loss of polar functional groups (oxygen-containing) in organic matter and the regular arrangement of carbon atoms, the polarity of organic matter molecules decreases, reducing the adsorption capacity of the organic matter to polar water molecules [53]. As shown in Figure 9(a), the water content in the shale reservoir decreases when the relative content of graphite structures increases. It indicates that the graphitization of organic matter reduces the adsorption sites of water and the deep shale's ability to adsorb water. In addition, the graphitization can result in a gradual increase in the density of carbon atoms on the surface of organic matter, making the structure distribution smoother and more continuous, thus enhancing the ability of organic matter to adsorb methane [54]. As shown in Figure 9(b), Langmuir volume is positively correlated with the relative content of graphite structures when the shale sample is moisture-equilibrated. Langmuir volume by the samples from Well Nx202 is higher than that adsorbed by the samples from Well H202 (Figure 5). This result suggests that graphitization in organic matter reduces the TSSA of deep shale, but not reduce the adsorption of methane by pores in organic matter due to the graphite structure's strong ability to adsorb methane.

5.2. Sealing Capacity of Deep Shale Reservoirs

5.2.1. Self-Sealing of Deep Shale Reservoirs. Self-sealing of shale gas reservoirs refers to the sealing effect on gas due to the weakened gas transport capacity in shale reservoirs resulting from the molecular forces within the gas or between the gas and the pore interface [55]. At the micro- and nano-scale, the flow of gas depends on the pore diameter and the free path of gas molecules [17, 19]. With a given free path of gas molecules, the smaller the pore size, the more frequent the interaction between the gas and the pore surface will be, and the weaker the gas transport capacity [17]. As shown in Table 3, the average pore diameter of deep shale reservoirs is distributed within a narrow range from 4.14 nm to 13.38 nm. The methane molecules with limited transport capacity mainly move through slip flow, overflow, and surface diffusion [17]. The diameter of pores in deep shale reservoirs is primarily determined by the contents of clay minerals and the graphitization degree (Figure 10). The higher the contents of clay minerals, the larger the average pore diameter will be (Figure 10(a)), which enhance the transport capacity of methane in deep shale reservoirs. The higher the graphitization degree, the smaller the average pore diameter will be (Figure 10(b)), inhibiting methane

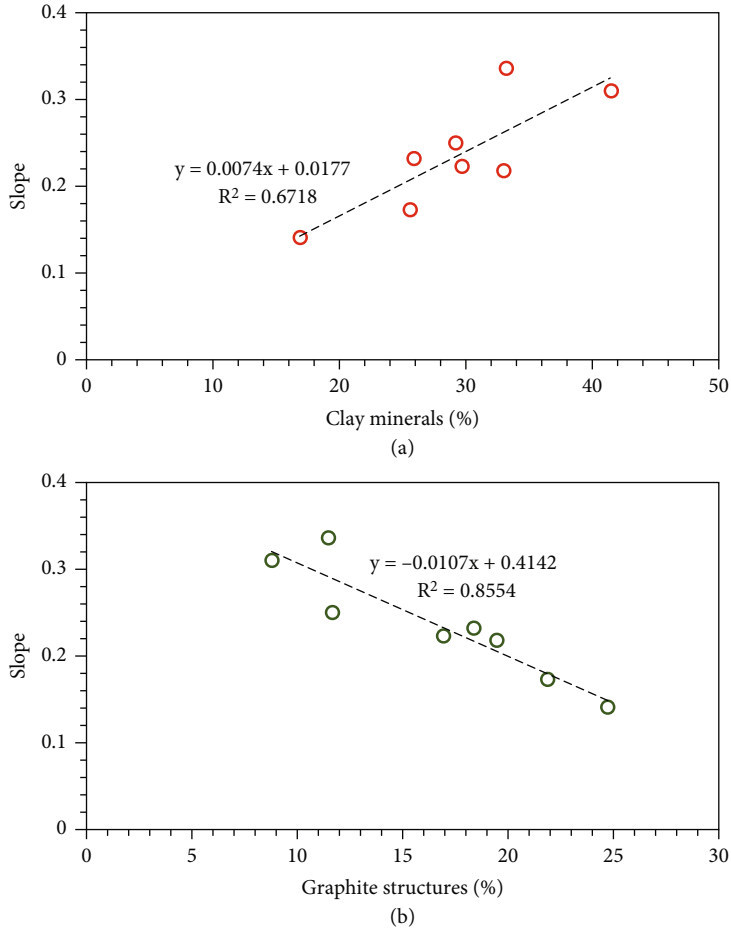

Figure 11: Spontaneous imbibition slope vs. contents of (a) clay mineral and (b) the relative content of graphite structures.

transport capacity in deep shale reservoirs and thereby enhancing their self-sealing ability.

5.2.2. Connectivity of Deep Shale Reservoir. The interconnected pores in shale reservoirs often provide good dissipation channels for shale gas [13]. The pore structure in deep shale reservoirs mainly depends on the clay minerals and the graphitization degree (Figure 11). As shown in Figure 11(a), the SI slope of the deep shale reservoir increases with the higher contents of clay minerals. The increase of clay minerals significantly improves the connectivity of deep shale reservoirs. The possible explanation may be that abundant intragranular pores and intercrystalline pores forming between layers of clay minerals in deep shale increase the possibility of connectivity between pores. As shown in Figure 11(b), the SI slope decreases with increasing the relative content of graphite structures, indicating a destructing effect of organic matter graphitization on the connectivity of deep shale reservoirs. This may be caused by the severe damage to organic matter pores by the graphitization of organic matter, resulting in a poor connection between previously well-connected pores in organic matter. It also can be seen from the higher TPV (Table 3) and lower porosity (Table 1) of these reservoirs. Despite the large TPV, the connected matrix pores are relatively small, indicating many of disconnected, isolated pores in the deep shale.

5.2.3. Contribution of Water to the Sealing Ability of Deep Shale Reservoirs. LF_I^4 deep shale reservoir is characterized by high contents of clay minerals and water (Figure 2). Sample 10 with relatively low contents of clay minerals and water were selected from LF_I^4 to conduct three repeated vertical bedding SI experiments. The results are shown in Figure 4. As the number of experiments increases, the SI slope gradually decreases, indicating that the connectivity of pores in deep shale reservoirs weakens after repeated experiments. This is maybe caused by the swelling effect of clay minerals adsorbing water, which changes the pore structure of shale samples and reduces pore connectivity [56]. In deep shale reservoirs with higher contents of water and clay minerals, pore connectivity may be destroyed even more seriously. The LF_I^4 deep shale reservoir has good pore connectivity and a larger pore diameter under dry conditions (Table 3). However, in a natural environment, the contained water limits methane's ability to transfuse or flow in the LF_I^4 shale reservoir and plays a role in preventing methane from dissipating from the lower shale reservoirs [57].

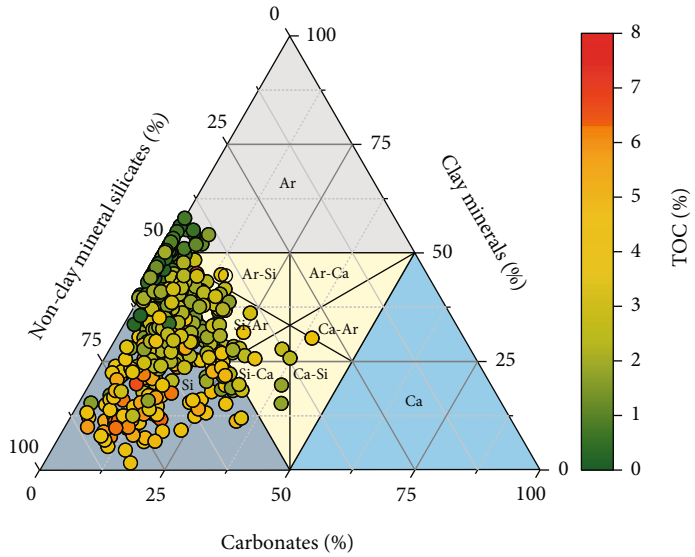

Figure 12: Ternary diagram showing the mineral composition, TOC content, and lithofacies classification of Longmaxi formation in the Sichuan Basin. Ar: argillaceous shale; Ca: calcareous shale; Si: siliceous shale.

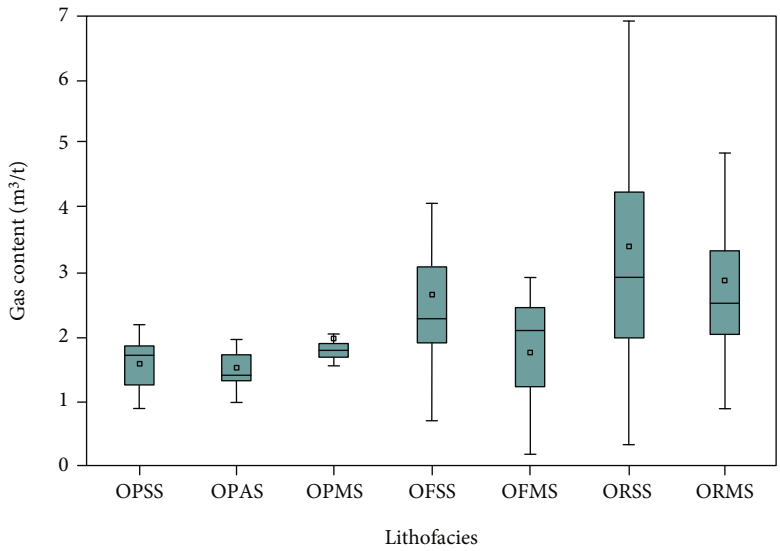

Figure 13: A box plot of shale gas content vs. shale lithofacies for the Longmaxi Formation.

5.3. Gas-Bearing Characteristics in Deep Shale Reservoirs

5.3.1. Lithofacies of Deep Shale Reservoirs and Their Gas-Bearing Characteristics. Shale lithofacies were classified based on the organic matter richness and mineral compositions [58]. According to the TOC content, shale could be divided into three types: organic-rich shale (TOC > 2%), organic-fair shale (2% > TOC > 1%), and organic-poor shale (TOC < 1%). According to the contents of non-clay mineral silicates (Si), clay minerals (Ar), and carbonates (Ca), shale could be classified into four types: argillaceous shale (clay minerals contents > 50%), siliceous shale (non-clay mineral silicates > 50%), calcareous shale (carbonates > 50%), and mixed shale (non-clay mineral silicates, carbonates, and clay minerals contents < 50%).

As shown in Figure 12, the distribution of deep shale lithofacies is mainly concentrated in seven types of lithofacies: organic-poor siliceous shale (OPSS), organic-poor argillaceous shale (OPAS), organic-poor mixed shale (OPMS), organic-fair siliceous shale (OFSS), organic-fair mixed shale (OFMS), organic-rich siliceous shale (ORSS), and organic-rich mixed shale (ORMS). Similar to shallow shale gas reservoirs, lithofacies with more enriched hydrocarbon generating materials tend to have higher gas content (Figure 13). On the one hand, abundant organic matter means that shale has good gas generating potential; on the other hand, nanoscale pores in organic matter are relatively developed, which increases the storage capacity of shale [21]. However, graphite structure of deep shale gas reservoir is generally developed. The difference in the

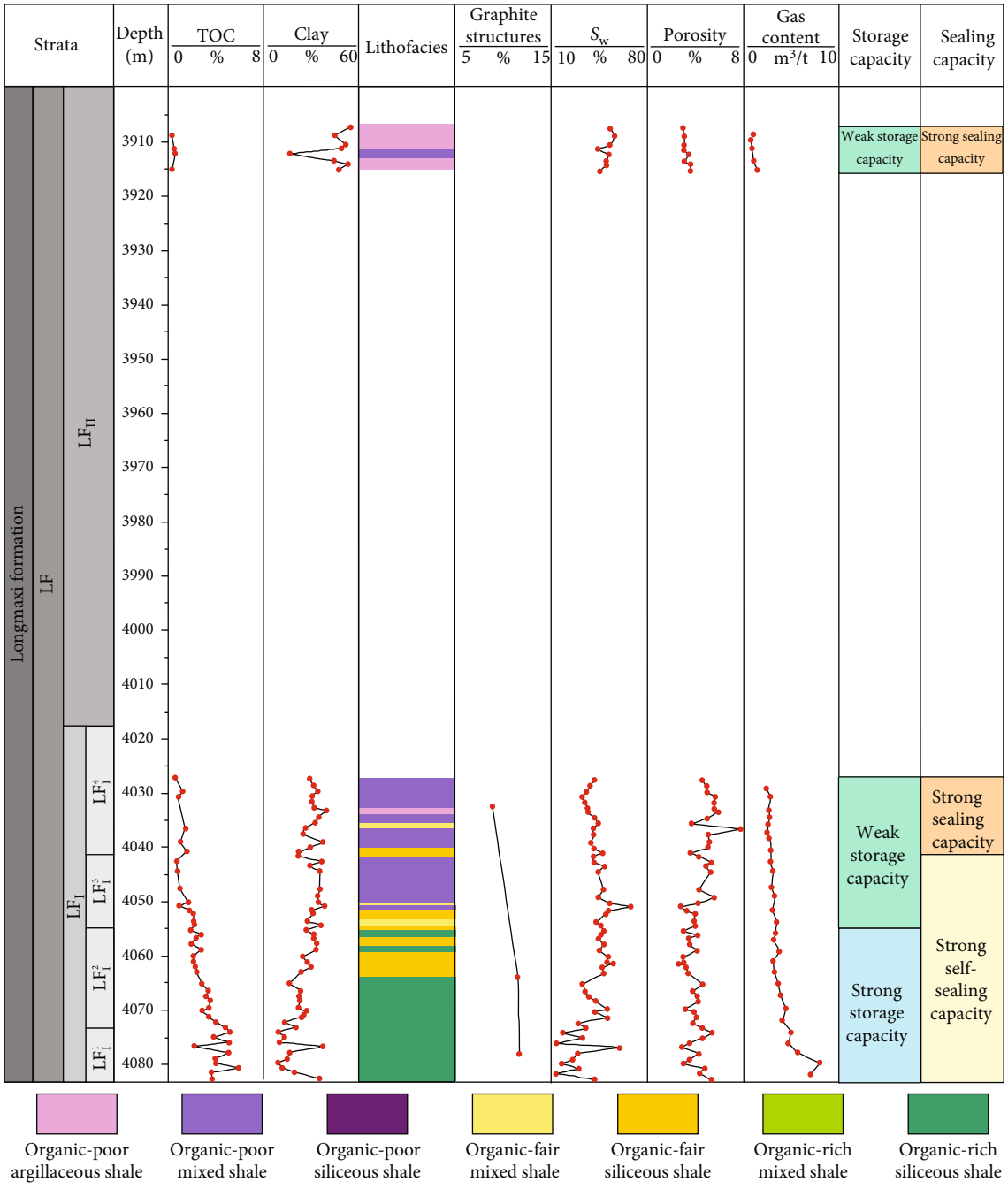

FIGURE 14: TOC, clay minerals contents, lithofacies, relative content of graphite structure, S_w, porosity, and gas content of Longmaxi formation of well H202. See Figure 1 for the well location.

development of graphite structure in the same lithofacies leads to the difference in the development of organic matter pores, which further leads to the wide distribution of gas content. At the same time, the lithofacies with high clay minerals contents often show low gas content (Figure 13). This is because the S_w in the deep shale reservoirs is high (Figure 2(f)), so that the hydrophilic clay mineral pores are often occupied by water. The shale lithofacies with high clay mineral contents have higher S_w and lower gas content.

5.3.2. Analysis of the Difference of Gas Bearing Characteristics. The capability of deep shale reservoir to store gas and seal gas and their spatial configuration relationship lead to significant differences in gas bearing characteristics. Well H202 is a typical high-yield well of deep shale gas, with a production rate of 22.37×10^4 m^3/d, and outstanding economic benefits for exploitation. Compared with Well H202, the production of deep shale gas from Well Nx202 is extremely low, with no economic value for its further exploitation.

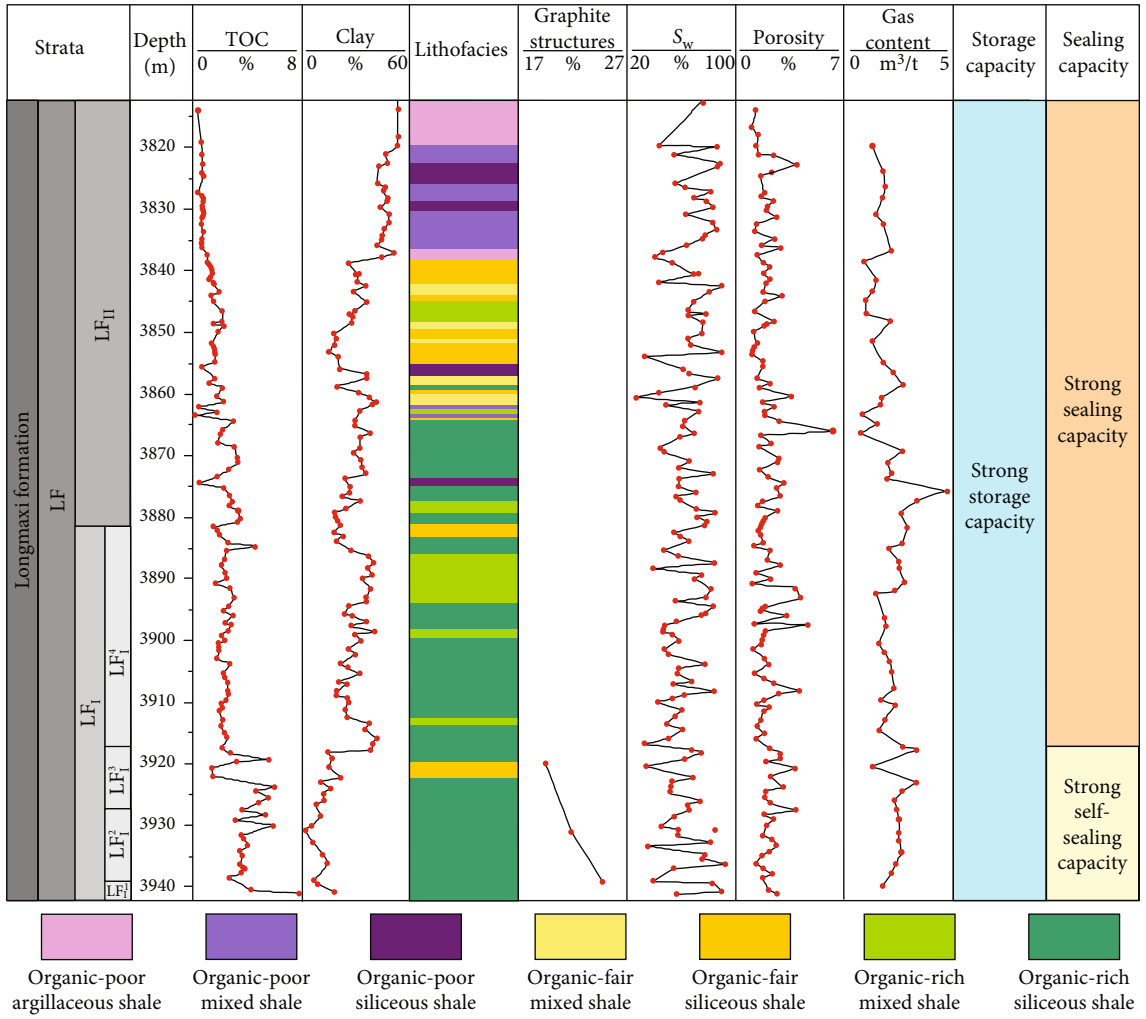

FIGURE 15: TOC, clay minerals contents, lithofacies, relative content of graphite structure, S_w, porosity, and gas content of Longmaxi formation of well Nx202. See Figure 1 for the well location.

As shown in Figure 14, the graphite structures in the samples from Well H202 are less developed, which enable the organic matter to resist elastic deformation and suffer less damage due to compaction. The proper graphitization degree can provide more adsorption sites for methane and thereby enhance the shale reservoir's ability to adsorb methane. LF_I^2 and LF_I^1 at Well H202 are mainly composed of ORSS and OFSS with low water content, resulting in less space for methane storage being occupied by water in the shale reservoirs. LF_I^2 and LF_I^1 samples from Well H202 show good storage capacity. From LF_I^3 to LF_{II}, OPAS and OPMS appear more frequently. Due to the increased contents of clay minerals in the shale reservoir, the S_w in the shale reservoir increases continuously from LF_I^3 to LF_{II}, and the contained water brings greater damage to shale gas storage space. The LF_I^3, LF_I^4, and LF_{II} shale reservoirs show a poor storage capacity. On the other hand, due to the high S_w and contents of clay minerals, the pore connectivity of shale reservoirs is severely damaged. LF_I^3, LF_I^4, and LF_{II} shale reservoirs can well seal the shale gas in the LF_I^2 and LF_I^1. The proper graphitization degree in the entire shale interval hampers the transmission capacity of shale gas in the reservoirs and enhances the self-sealing capacity of LF_I^2 and LF_I^1 shale reservoirs. The pattern of a lower shale reservoirs with good microstorage and microself-sealing capacity and an upper shale reservoirs with good microsealing capacity brings high gas content for the lower shale reservoirs.

As shown in Figure 15, the deep shale reservoirs of Well Nx202 are highly graphitized. Under the pressure of the upper formations, the organic matter is susceptible to plastic deformation leading to severe damage to the pores. The LF_{II} and LF_I of Well Nx202 have higher S_w. Although the layer LF_I is dominated by ORMS and ORSS, water seriously occupies the accumulation and storage space for methane, causing severe damage to the storage capacity of these layers. There are abundant OFSS, OFMS, OPAS, and OPMS in LF_{II}. Due to the high S_w, the gas storage space and connectivity of LF_{II} are destroyed. The lower shale reservoir shows low gas content due to the insufficient storage capacity of the lower shale reservoir.

The data analysis results of the seven deep shale gas wells show that a good gas storage capacity could be defined as a

TOC > 1%, clay minerals < 38%, a low water content (i.e., S_w < 50%), and a low graphitization degree of organic matter (<20%). An excellent microsealing capacity is usually defined as the TOC < 1%, clay minerals > 37%, with relatively high water content (S_w > 50%), and a medium graphitization degree of organic matter (>5%). The four deep shale gas wells (L201, L204, H202, and Z202) with high gas content show similar patterns, including good microstorage and self-sealing capacity in the lower shale reservoir and good microsealing capacity in the upper shale reservoir.

6. Conclusions

(1) Compared with shallow shale reservoirs, deep shale reservoirs have lower porosity, higher water saturation, lower gas content, higher graphitization degree, and stronger methane adsorption capacity

(2) In deep shale reservoirs with a higher degree of graphitization, organic matter has a relatively weak ability to resist elastic deformation, and the organic matter pores often deform or even collapse after being squeezed. As a result, the gas storage in these shale reservoirs is severely damaged, hindering gas preservation. In shale reservoirs with a lower degree of graphitization, the graphite structures can enhance the ability of the shale reservoir to adsorb gas and realize self-sealing, facilitating gas preservation

(3) Higher contents of clay minerals in deep shale reservoirs can greatly increase the pore volume and specific surface area. However, the affinity of clay minerals for water can lead to an increase in water content in shale reservoirs, hindering the capacity of shale reservoirs to store and transport shale gas. Under this effect, the upper shale reservoir with higher contents of clay mineral shows outstanding sealing performance for the lower shale reservoir, helping it preserve shale gas

(4) It is necessary for high gas content in deep shale reservoirs that good storage and self-sealing capacity of the lower shale reservoirs and good sealing capacity of the upper shale reservoirs

Data Availability

The data that support the findings of this study are available from the corresponding author upon reasonable request.

Conflicts of Interest

There are no conflicts of interest with respect to the results of this paper.

Acknowledgments

We thank PetroChina Southwest Oil and Gas field Company for providing samples and data access and for granting permission to publish this work. This work was financially supported by the National Natural Science Foundation of China (Grant no. 41972147 and no. 42072151), and we thank the sponsors of these projects.

References

[1] J. B. Curtis, "Fractured shale-gas systems," *AAPG Bulletin*, vol. 86, no. 11, pp. 1921–1938, 2002.

[2] C. Zou, D. Dong, S. Wang et al., "Geological characteristics and resource potential of shale gas in China," *Petroleum Exploration and Development*, vol. 37, no. 6, pp. 641–653, 2010.

[3] U. Kuila and M. Prasad, "Specific surface area and pore-size distribution in clays and shales," *Geophysical Prospecting*, vol. 61, no. 2, pp. 341–362, 2013.

[4] A. A. Hinai, R. Rezaee, L. Esteban, and H. J. Dargahi, "Assessment of shale gas pore systems," *The APPEA Journal*, vol. 54, no. 2, p. 531, 2014.

[5] L. Zhang, Z. Li, and R. Zhu, "The formation and exploitation of shale gas," *Natural Gas Industry*, 2009.

[6] Y. Lu, S. Jiang, Y. Lu, S. Xu, Y. Shu, and Y. Wang, "Productivity or preservation? The factors controlling the organic matter accumulation in the late Katian through Hirnantian Wufeng organic-rich shale, South China," *Marine and Petroleum Geology*, vol. 109, pp. 22–35, 2019.

[7] R. Y. Wang, W. L. Ding, Y. Q. Zhang et al., "Analysis of developmental characteristics and dominant factors of fractures in Lower Cambrian marine shale reservoirs: a case study of Niutitang formation in Cen'gong block, southern China," *Journal of Petroleum Science and Engineering*, vol. 138, pp. 31–49, 2016.

[8] P. Wang, Z. Jiang, L. Yin et al., "Lithofacies classification and its effect on pore structure of the Cambrian marine shale in the Upper Yangtze Platform, South China: evidence from FE-SEM and gas adsorption analysis," *Journal of Petroleum Science & Engineering*, vol. 156, pp. 307–321, 2017.

[9] L. Q. Zhu, C. M. Zhang, Z. S. Zhang, and X. Zhou, "High-precision calculation of gas saturation in organic shale pores using an intelligent fusion algorithm and a multi-mineral model," *Advances in Geo-Energy Research*, vol. 4, no. 2, pp. 135–151, 2020.

[10] W. Ji, Y. Song, Z. Jiang, X. Wang, Y. Bai, and J. Xing, "Geological controls and estimation algorithms of lacustrine shale gas adsorption capacity: a case study of the Triassic strata in the southeastern Ordos Basin, China," *International Journal of Coal Geology*, vol. 134-135, pp. 61–73, 2014.

[11] Z. Jiang, S. Yan, T. L. Xiang et al., "Controlling factors of marine shale gas differential enrichment in southern China," *Petroleum Exploration and Development*, vol. 47, no. 3, pp. 661–673, 2020.

[12] K. Zhang, Y. Song, S. Jiang et al., "Shale gas accumulation mechanism in a syncline setting based on multiple geological factors: an example of southern Sichuan and the Xiuwu Basin in the Yangtze Region," *Fuel*, vol. 241, pp. 468–476, 2019.

[13] K. Zhang, C. Jia, Y. Song et al., "Analysis of lower Cambrian shale gas composition, source and accumulation pattern in different tectonic backgrounds: a case study of Weiyuan block in the upper Yangtze region and Xiuwu Basin in the lower Yangtze region," *Fuel*, vol. 263, article 115978, 2020.

[14] S. Long, D. Feng, F. Li, and W. du, "Prospect analysis of the deep marine shale gas exploration and development in the Sichuan Basin, China," *Journal of Natural Gas Geoscience*, vol. 3, no. 4, pp. 181–189, 2018.

[15] X. Ma, H. Wang, S. Zhou, Z. Shi, and L. Zhang, "Deep shale gas in China: geological characteristics and development strategies," *Energy Reports*, vol. 7, no. 6, pp. 1903–1914, 2021.

[16] W. Shen, X. Li, T. Ma, J. Cai, X. Lu, and S. Zhou, "High-pressure methane adsorption behavior on deep shales: experiments and modeling," *Physics of Fluids*, vol. 33, no. 6, article 063103, 2021.

[17] K. Wu and Z. Chen, "Review of gas transport in nanopores in shale gas reservoirs," *Petroleum Science Bulletin*, vol. 1, no. 1, pp. 91–127, 2016.

[18] F. Javadpour, D. Fisher, and M. Unsworth, "Nanoscale gas flow in shale gas sediments," *Journal of Canadian Petroleum Technology*, vol. 46, no. 10, pp. 55–61, 2007.

[19] K. Wu, Z. Chen, and X. Li, "Real gas transport through nanopores of varying cross-section type and shape in shale gas reservoirs," *Chemical Engineering Journal*, vol. 281, pp. 813–825, 2015.

[20] X. Wang, Z. Jiang, S. Jiang et al., "Pore evolution and formation mechanism of organic-rich shales in the whole process of hydrocarbon generation: study of artificial and natural shale samples," *Energy & Fuels*, vol. 34, no. 1, pp. 332–347, 2020.

[21] X. Tang, Z. Jiang, S. Jiang, P. Wang, and C. Xiang, "Effect of organic matter and maturity on pore size distribution and gas storage capacity in high-mature to post-mature shales," *Energy & Fuels*, vol. 30, no. 11, pp. 8985–8996, 2017.

[22] F. Hao, H. Zou, and Y. Lu, "Mechanisms of shale gas storage: implications for shale gas exploration in China," *AAPG Bulletin*, vol. 97, no. 8, pp. 1325–1346, 2013.

[23] X. Guo, D. Hu, Y. Li, R. Liu, and Q. Wang, "Geological features and reservoiring mode of shale gas reservoirs in Longmaxi Formation of the Jiaoshiba Area," *Acta Geologica Sinica-English Edition*, vol. 88, no. 6, pp. 1811–1821, 2014.

[24] C. Zou, Z. Yang, J. Dai et al., "The characteristics and significance of conventional and unconventional Sinian-Silurian gas systems in the Sichuan Basin, central China," *Marine & Petroleum Geology*, vol. 64, pp. 386–402, 2015.

[25] H. Nie, Q. Chen, G. Zhang, C. Sun, P. Wang, and Z. Lu, "An overview of the characteristic of typical Wufeng-Longmaxi shale gas fields in the Sichuan Basin, China," *Natural Gas Industry B*, vol. 8, no. 3, pp. 217–230, 2021.

[26] Y. Li, D. He, L. Chen, Q. Mei, C. Li, and L. Zhang, "Cretaceous sedimentary basins in Sichuan, SW China: restoration of tectonic and depositional environments," *Cretaceous Research*, vol. 57, pp. 50–65, 2016.

[27] S. G. Liu, B. Deng, Y. Zhong et al., "Unique geological features of burial and superimposition of the lower paleozoic shale gas across the Sichuan basin and its periphery," *Earth Science Frontiers*, vol. 23, no. 1, pp. 11–28, 2016.

[28] J. C. Zhang, H. K. Nie, B. Xu, S. L. Jiang, and P. X. Zhang, "Geological condition of shale gas accumulation in Sichuan Basin," *Natural Gas Industry*, vol. 28, no. 2, pp. 151–156, 2008.

[29] X. S. Guo, *Enrichment Mechanism and Exploration Technology of Jiaoshiba Block in Fuling Shale Gas Field*, Science Press, Beijing, China, 2014.

[30] B. He, Y. G. Xu, Y. M. Wang, Z. Y. Luo, and K. M. Wang, "The magnitude of crustal uplift prior to the eruption of the Emeishan basalt: inferred from sedmenentary records," *Geotectonica et Metallogenia*, vol. 29, pp. 316–320, 2005.

[31] Y. Wang, H. Wang, Z. Qiu et al., "Basic characteristics of key interfaces in Upper Ordovician Wufeng Formation - Lower Silurian Longmaxi Formation in Sichuan Basin and its periphery, SW China," *Petroleum Exploration and Development*, vol. 49, no. 1, pp. 37–51, 2022.

[32] X. Ma and J. Xie, "The progress and prospects of shale gas exploration and development in southern Sichuan Basin, SW China," *Petroleum Exploration and Development*, vol. 45, no. 1, pp. 172–182, 2018.

[33] X. Ma, H. Wang, S. Zhou, Z. Feng, H. Liu, and W. Guo, "Insights into NMR response characteristics of shales and its application in shale gas reservoir evaluation," *Journal of Natural Gas Science and Engineering*, vol. 84, article 103674, 2020.

[34] R. Wang, Z. Hu, S. Long et al., "Differential characteristics of the Upper Ordovician-Lower Silurian Wufeng- Longmaxi Shale Reservoir and its implications for exploration and development of shale gas in/around the Sichuan Basin," *Acta Geologica Sinica (English edition)*, vol. 93, no. 3, pp. 520–535, 2019.

[35] Z. Huang, T. Liang, Z. W. Zhan, Y. R. Zou, M. Li, and P. Peng, "Chemical structure evolution of kerogen during oil generation," *Marine and Petroleum Geology*, vol. 98, pp. 422–436, 2018.

[36] Z. Xue, Z. Jiang, X. Wang et al., "Genetic mechanism of low resistivity in high-mature marine shale: insights from the study on pore structure and organic matter graphitization," *Marine and Petroleum Geology*, vol. 144, article 105825, 2022.

[37] Q. Y. Lin, T. Q. Li, Z. J. Liu et al., "High-resolution TEM observations of isolated rhombohedral crystallites in graphite blocks," *Carbon*, vol. 50, no. 6, pp. 2369–2371, 2012.

[38] S. Brunauer, P. H. Emmett, and E. Teller, "Adsorption of gases in multimolecular layers," *Journal of the American Chemical Society*, vol. 60, no. 2, pp. 309–319, 1938.

[39] E. P. Barrett, L. G. Joyner, and P. P. Halenda, "The determination of pore volume and area distributions in porous substances. I. Computations from nitrogen isotherms," *Journal of The American Chemical*, vol. 73, no. 1, pp. 373–380, 1951.

[40] Z. Gao and Q. Hu, "Initial water saturation and imbibition fluid affect spontaneous imbibition into Barnett shale samples," *Journal of Natural Gas Science and Engineering*, vol. 34, pp. 541–551, 2016.

[41] L. Handy, "Determination of effective capillary pressures for porous media from imbibition data," *Aime*, vol. 219, no. 1, pp. 75–80, 1960.

[42] W. Ji, Y. Song, Z. Jiang et al., "Estimation of marine shale methane adsorption capacity based on experimental investigations of lower Silurian Longmaxi formation in the upper Yangtze platform, South China," *Marine and Petroleum Geology*, vol. 68, pp. 94–106, 2015.

[43] M. R. Yassin, M. Begum, and H. Dehghanpour, "Organic shale wettability and its relationship to other petrophysical properties: a Duvernay case study," *International Journal of Coal Geology*, vol. 169, pp. 74–91, 2017.

[44] M. H. Sayyouh, A. S. Dahab, and A. E. Omar, "Effect of clay content on wettability of sandstone reservoirs," *Journal of Petroleum Science & Engineering*, vol. 4, no. 2, pp. 119–125, 1990.

[45] Y. Ma, N. Zhong, D. Li, Z. Pan, L. Cheng, and K. Liu, "Organic matter/clay mineral intergranular pores in the Lower Cambrian Lujiaping Shale in the north-eastern part of the upper Yangtze area, China: a possible microscopic mechanism for gas preservation," *International Journal of Coal Geology*, vol. 137, pp. 38–54, 2015.

[46] E. G. Witte, H. J. Schenk, P. J. Müller, and K. Schwochau, "Structural modifications of kerogen during natural evolution

as derived from 13C CP/MAS NMR, IR spectroscopy and rock-eval pyrolysis of Toarcian shales," *Organic Geochemistry*, vol. 13, no. 4-6, pp. 1039–1044, 1998.

[47] Y. Zheng, C. Jiang, and Y. Liao, "Relationship between hydrocarbon gas generation and kerogen structural evolution revealed by closed system pyrolysis and quantitative Py-GC analysis of a type II kerogen," *Energy & Fuels*, vol. 35, no. 1, pp. 251–263, 2021.

[48] Y. Hou, K. Zhang, F. Wang et al., "Structural evolution of organic matter and implications for graphitization in overmature marine shales, south China," *Marine and Petroleum Geology*, vol. 109, pp. 304–316, 2019.

[49] C. A. Coulson, S. Senent, M. A. Herraez, M. Leal, and E. Santos, "Deformation of graphite lattices by interstitial carbon atoms," *Carbon*, vol. 3, no. 4, pp. 445–457, 1966.

[50] Y. M. Wang, D. Z. Dong, H. Yang et al., "Quantitative characterization of reservoir space in the lower Silurian Longmaxi shale, southern Sichuan, China," *Science China Earth Science*, vol. 57, pp. 1348–1356, 2014.

[51] D. Zhu, Z. Jiang, S. Jiang et al., "Water-bearing characteristics and their influences on the reservoir capacity in terrestrial shale reservoirs: a case study of the lower Jurassic Ziliujing Formation in the Northeast Sichuan Basin, China," *Marine and Petroleum Geology*, vol. 123, article 104738, 2021.

[52] D. Silva, M. Lopes, J. L. Martins, M. M. Ramos, and R. Bijani, "Estimation of clay minerals from an empirical model for cation exchange capacity: an example in Namorado oilfield, Campos Basin, Brazil," *Applied Clay Science*, vol. 158, pp. 195–203, 2018.

[53] J. Zhou, Q. Mao, and K. H. Luo, "Effects of moisture and salinity on methane adsorption in kerogen: a molecular simulation study," *Energy & Fuels*, vol. 33, no. 6, pp. 5368–5376, 2019.

[54] T. Zhao, X. Li, H. Zhao, and M. Li, "Molecular simulation of adsorption and thermodynamic properties on type II kerogen: influence of maturity and moisture content," *Fuel*, vol. 190, pp. 198–207, 2017.

[55] C. Jia, X. Pang, and Y. Song, "The mechanism of unconventional hydrocarbon formation: Hydrocarbon self- sealing and intermolecular forces," *Petroleum Exploration and Development*, vol. 48, no. 3, pp. 507–526, 2021.

[56] Z. Gao and Q. Hu, "Pore structure and spontaneous imbibition characteristics of marine and continental shales in China," *AAPG Bulletin*, vol. 102, no. 10, pp. 1941–1961, 2018.

[57] F. Yang, S. Xu, F. Hao et al., "Petrophysical characteristics of shales with different lithofacies in Jiaoshiba area, Sichuan Basin, China: implications for shale gas accumulation mechanism," *Marine and Petroleum Geology*, vol. 109, pp. 394–407, 2019.

[58] F. Yang, B. L. Yu, and S. Xu, "Water sorption and transport in shales: an experimental and simulation study," *Water Resources Research*, vol. 57, no. 2, article e2019WR026888, 2021.